The cosmic 21-cm revolution: charting the first billion years of our Universe

Andrei Mesinger

August 4, 2019

Contents

Preface

This set of files can be used to create your typescript in LaTeX. You can add packages as necessary.

Remember that references need to be at the chapter level and you may find the package chapterbib useful for this.

About the Author

Remember to include a brief biography of the Authors or Editors, including a photo.

Contributors

Gianni Bernardi
INAF - Istituto di Radio Astronomia
via Gobetti 101, 40129, Bologna, Italy &
Department of Physics and Electronics
Rhodes University
PO Box 94, Grahamstown, 6140, South Africa

Lincoln J. Greenhill
Harvard-Smithsonian Center for Astrophysics
60 Garden St, Mail Stop 42
Cambridge, MA 02138 USA

Bradley Greig
School of Physics
The University of Melbourne
Parkville, Melboune VIC, Australia

Vibor Jelić
Ruđer Bošković Institute
Zagreb, Croatia

Peter Jones
Department of Physics
University of New England
Acadia, Maine, USA

Jonathan Pritchard
Blackett Laboratory
Imperial College
London, UK

Simon Smith
Department of Electrical Engineering
University of Oxbridge, Camford, USA

Cathryn M. Trott

International Centre for Radio Astronomy Research
Curtin University, Bentley WA, Australia

Chapter 1

21 cm observations: calibration, strategies, power spectra and images

Gianni Bernardi (INAF-IRA & Rhodes University)

Abstract

This chapter reviews the basics of radio interferometry (van-Citter-Zernike theorem, uv-coverage, image formation calibration) and how they are linked to the measurements of the 21-cm power spectrum and its tomography

1.1 Interferometry overview

The Van Cittert-Zernike theorem expresses the fundamental relationship between the sky spatial brightness (or brightness distribution) I and the quantity measured by an interferometer, i.e. the visibility V (e.g., [68]):

$$V_{ij}(\mathbf{b},\lambda) = \int_{\Omega} \bar{I}(\hat{\sigma},\lambda)\, e^{-2\pi i \mathbf{b}\cdot\hat{\sigma}} d\sigma, \tag{1.1}$$

where $\mathbf{b}$ is the baseline vector that separates antenna i and antenna j, and $\hat{sigma}$ is the observing direction (see Figure 1.1) and the integral is taken over the source size Ω. The baseline vector is here specified in wavelengths, i.e. $\mathbf{b} = \frac{\mathbf{b}_{\rm m}}{\lambda}$, where $\mathbf{b}_{\rm m}$ is the baseline vector expressed in meters and λ is the observing wavelength. It can be seen in Figure 1.1, that the celestial signal travels an extra path between the two antennas, and that length corresponds to a geometrical time delay $\tau = \mathbf{b}\cdot\hat{\sigma}$, where the word "geometrical" refers to the fact that the delay depends upon the source position in the sky and the relative separation between the two antennas.

The sky brightness distribution does not enter directly in equation 1.1, but filtered by the antenna primary beam response A that depends upon the direction in the sky and the wavelength, i.e. $\bar{I}(\mathbf{b},\lambda) = A(\mathbf{b},\lambda)\, I(\mathbf{b},\lambda)$. The response of the primary beam attenuates the sky emission away from the pointing direction, effectively reducing the field of view θ of the instrument. Generally speaking, the size of the field of view is essentially given by the

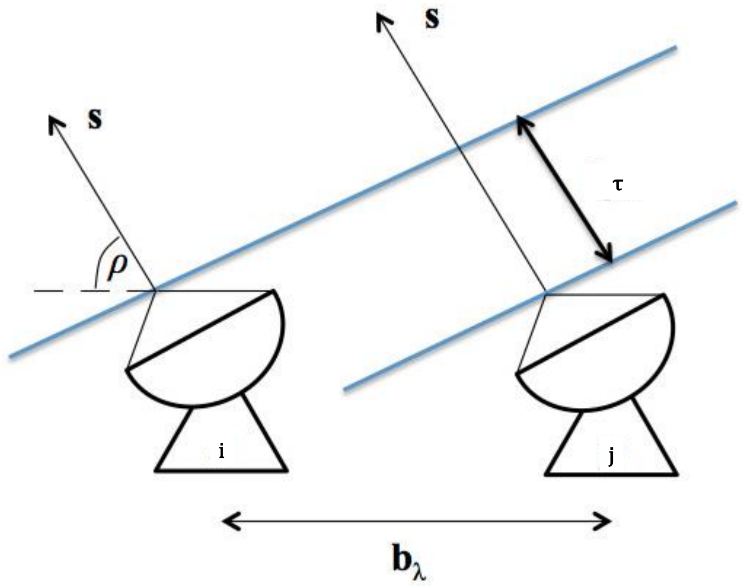

Figure 1.1: A standard schematic of the two element interferometer.

antenna diameter D:

$$\theta \approx \frac{\lambda}{D}. \tag{1.2}$$

Equation 1.1 is often re-written in a different coordinate system, i.e. using the components of the baseline vector (u,v,w) and the reciprocal (l,m,n), where (l,m) are the coordinates in the plane on the sky tangent to the observing direction n (for a detailed discussion of coordinate systems see, for example [68]). Using this coordinate system, equation 1.1 becomes (e.g., [68]):

$$V_{ij}(u,v,w,\lambda) = \int_{\Omega} \bar{I}(l,m,\lambda)\, e^{-2\pi i(ul+vm+w(n-1))} \frac{dl\,dm\,dn}{\sqrt{1-l^2-m^2}}, \tag{1.3}$$

Although low frequency radio observations are intrinsically wide-field, for the purpose of studying the 21 cm observables, we can reduce equation 1.3 to a two dimensional Fourier transform:

$$V_{ij}(u,v,\lambda) = \int_{\Omega} \bar{I}(l,m,\lambda)\, e^{-2\pi i(ul+vm)} dl\,dm. \tag{1.4}$$

Equation 1.4 indicates that an *interferometer measures the two dimensional Fourier transform of the spatial sky brightness distribution*. If our goal is to reconstruct the sky brightness distribution, equation 1.4 can be inverted into its corresponding Fourier pair:

$$\bar{I}(l,m,\lambda) = \int V_{ij}(u,v,\lambda)\, e^{2\pi i(ul+vm)} du\,dv. \tag{1.5}$$

Equation 1.5 is, however, a poor reconstruction of the sky brightness distribution as only one Fourier mode is sampled at a single time instance. Strictly speaking, indeed, all the quantities in equation 1.4 and 1.5 are time variable. In most cases, the time dependence of the primary beam and the sky brightness distribution can be neglected, however, this is not the case for the visibility V as the projection of the baseline vector with respect to the source direction changes significantly throughout a long (e.g. a few hours) track. In this way, many measurements of the visibility coherence function V can be made as (u,v) change with time, allowing for a better reconstruction of the $\bar{I}(l,m,\lambda)$ function. This methods is commonly referred to as *filling the uv plane via Earth rotation synthesis* and was invented by [57]. The other (complementary) way to fill the *uv* plane is to deploy more antennas on the ground in order to increase the number of instantaneous measurements of independent Fourier modes. If N antennas are connected in an interferometric array, $\frac{N(N-1)}{2}$ instantaneous measurements are made.

The combination of a large number of antennas and the Earth rotation synthesis, defines the sampling function $S(u,v)$ in the *uv* plane. In any real case, equation 1.5 can therefore be re-written as:

$$\bar{I}_D(l,m,\lambda) = \int S(u,v,\lambda)V(u,v,\lambda)\,e^{2\pi i(ul+vm)}du\,dv, \tag{1.6}$$

where $\bar{I}_D$ indicates the sky brightness distribution sampled at a finite number of (u,v) points (often termed *dirty image*) and where the explicit dependence on the antenna pair was dropped for simplicity. Using the convolution theorem, equation 1.6 can be re-written as:

$$\bar{I}_D(l,m,\lambda) = \tilde{SV} = \tilde{S} * \tilde{V} = \mathrm{PSF}(l,m,\lambda) * \tilde{V}(l,m,\lambda), \tag{1.7}$$

where the tilde indicates the Fourier transform, $*$ the convolution operation and PSF is the Point Spread Function, i.e. the response of the interferometric array to a point sources which, in our case, is also the Fourier transform of the *uv* coverage.

The sampling function always effectively reduces the integral over a finite (often not contiguous) area of the *uv* plane. In particular, the sampled *uv* plane is restricted to a minimum *uv* distance that cannot be shorter than the antenna[1] size and the largest separation between antennas, i.e. the maximum baseline $\mathbf{b}_{\mathrm{max}}$. The maximum baseline also sets the maximum angular resolution θ_b:

$$\theta_b \approx \frac{\lambda}{|\mathbf{b}_{\mathrm{max}}|}. \tag{1.8}$$

The incomplete sampling of the *uv* space leads to a PSF that has "sidelobes", i.e. nulls and secondary lobes that can often contaminate fainter true sky emission. The best reconstruction of the sky brightness distribution $\bar{I}$ requires deconvolution of the dirty image from the PSF.

1.2 21 cm observables: power spectra and images

The ultimate goal of 21 cm observations is to image the spatial distribution of the 21 cm signal as a function of redshift, also known as *21 cm tomography*. Given the curent theoretical predictions, such observations need to achieve mK sensitivity on a few arcminute angular scales (see Chapter 1 in this book). Most of the current arrays, however, only have

[1] In this chapter I use the words "antenna" and "station" interchangeably to indicate the correlated elements even if, in the literature, they are normally used to indicate a dish and and a dipole, or a cluster of dipoles, respectively.

the sensitivity to perform a statistical detection of the 21 cm signal, i.e. to measure its power spectrum. Given an intensity field T, function of the three dimensional spatial coordinate $\mathbf{x}$, its power spectrum $P(k)$ is defined as:

$$\langle \tilde{T}^*(\mathbf{k})\tilde{T}(\mathbf{k}')\rangle = (2\pi)^3 P(k)\delta^3(\mathbf{k}-\mathbf{k}') \tag{1.9}$$

where $\langle\rangle$ indicates the ensamble average, $\mathbf{k}$ is the Fourier conjugate of $\mathbf{x}$, tilde the Fourier transform, * the conjugate operator and δ the Dirac delta function. In 21 cm observations, power spectra can be computed directly from interferometric image cubes after deconvolution of the dirty image $\bar{I}_D(l,m,\lambda)$ from the point spread function (e.g., [51], [25], [5], [48]). Alternatively, the 21 cm power spectrum can be estimated directly from the interferometric visibilities. Equation 1.4 already shows that the interferometer is a "natural" spatial power spectrum instrument (e.g., [72]). Visibilities can be further Fourier transformed along the frequency axis (the so-called *delay trasform*, [47]):

$$\tilde{V}_{ij}(u,v,\tau) = \int_B \bar{I}(l,m,\nu)\, e^{-2\pi i\nu\tau} d\nu \tag{1.10}$$

where B is the observing bandwidth and τ is the geometrical delay. The delay transform is therefore proportional to the three dimensional power spectrum ([46]):

$$P(k) \propto \tilde{V}_{ij}(|\mathbf{b}|,\tau), \tag{1.11}$$

where the proportionality constant transforms the visibility units into power units ([46]). The observer units $(\mathbf{b},\tau)$ map directly in k modes parallel and perpendicular to the line of sight (e.g., [42]):

$$k_\perp = \frac{2\pi|\mathbf{b}|}{D_c} = \frac{2\pi\sqrt{u^2+v^2}}{D_c}, \quad k_\parallel = \frac{2\pi f_{21} H_0 E(z)}{c\,(1+z)^2}\,\tau, \tag{1.12}$$

where D_c is the transverse comoving distance, $f_{21} = 1421$ MHz, H_0 is the Hubble constant and $E(z) = \sqrt{\Omega)m(1+z)^3+\Omega_k(1+z)^2+\Omega_\Lambda}$. Due to the dependence of the geometrical delay upon frequency, equation 1.11 is only valid for short baselines, typically shorter than a few hundresd meters, for which the geometrical delay is fairly constant across the bandwidth and lines of constant $k_\parallel$ are essentially orthogonal to the $k_\perp$ axis ([46]).

Equation 1.10 does not only provide a link between visibilities and three dimensional power spectra, but also introduces the concept of "horizon limit", i.e. the maximum physical delay allowed $\tau_{\max} = \frac{|\mathbf{b}|}{c}$, where c is the speed of light. The most relevant implication of the existence of an horizon limit is the definition of a region in the two dimensional $(k_\parallel, k_\perp)$ power spectrum space where smooth-spectrum foregrounds are confined, leaving the remaining area uncontaminated in order to measure the 21 cm signal (the so-called "Epoch of Reionization (EoR) window", Figure 1.2). Foregrounds can therefore be "avoided" with no requirements for subtraction (e.g., [41], [71], [53], [69]; see also Chapter 6 in this book). The choice of a foreground avoidance strategy versus subtraction plays an important role in planning an experiment, its related observing strategy and the array calibration strategy.

The requirements for image tomography are the same as for high brightness sensitivity observations of diffuse emission like the Cosmic Microwave Background (e.g., [23], [17], [56]). The 21 cm spatial distribution throughout cosmic reionization has structures on 5-10

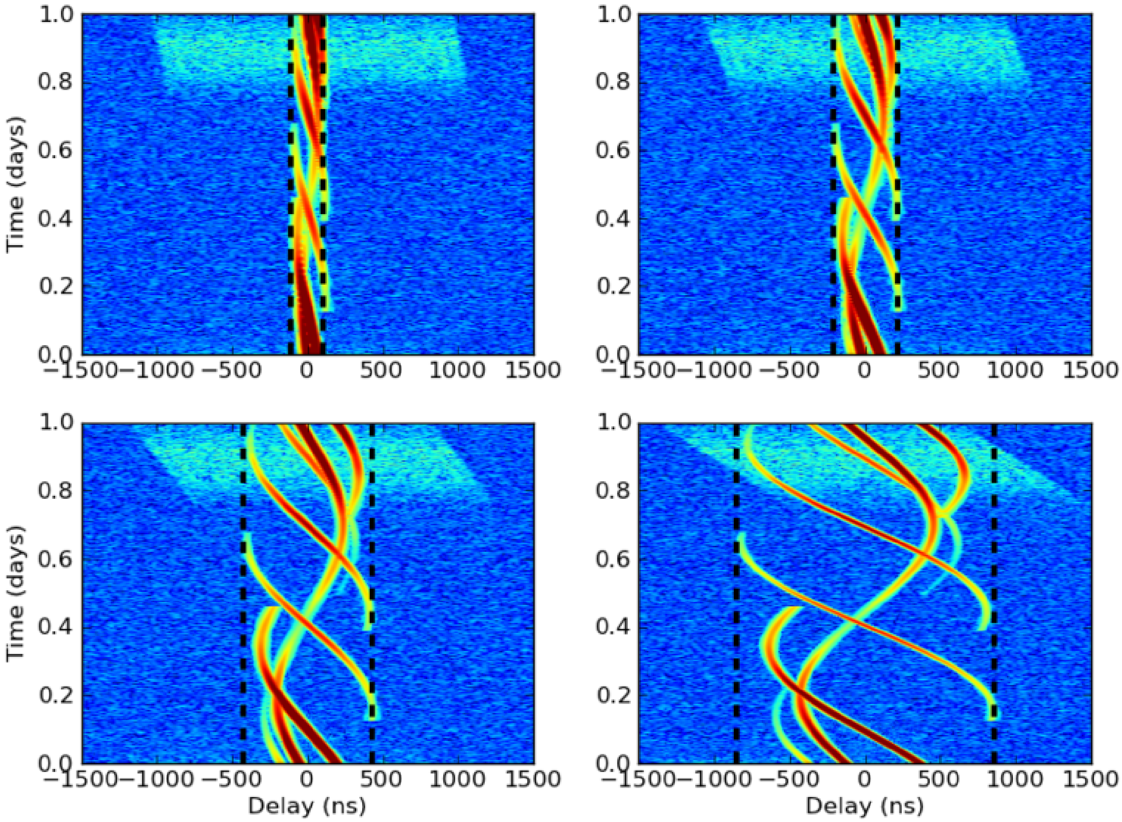

Figure 1.2: Amplitude of delay transformed visibilities as a function of time and delay for a 32 (top let), 64 (top right), 128 (bottom left) and 256 m (bottom right) baselines respectively (from [47]). A number of smooth spectrum point sources are simulated as foregrounds and their tracks are clearly bound within the horizon limit (black dashed line). The cyan emission is a fiducial 21 cm model that has power up to high delays regardless of the baseline length.

arcminutes up to degree scales (e.g., [14], [37], [33]). In order to image 21 cm fluctuations, a maximum baseline of the order of a few km gives a resolution of a few arcminutes in the $100-200$ MHz range, together with filled uv plane in order to accurately reconstruct their complex spatial structure. A filled uv plane also leads to a PSF with very low sidelobes, making the deconvolution process easier. The most stringent requirements for image tomography remain the accurate foregrond separation and, as I will review in the next section, the related instrumental calibration.

1.3 Interferometric calibration and 21 cm observations

Celestial radio signals always experience a corruption when observed with an interferometric array, due to the non-ideal instrumental response that is corrected in post processing in a process that is known as interferometric calibration. Calibration relies on the definition of a data model where the corruptions are described by antenna based quantities known as Jones matrices. Such data model is known as the interferometric measurement equation ([24],[60],[61],[62]).

If antenna 1 and antenna 2 measure two orthogonal, linear polarizations x and y, the cross-polarization visibility products can be grouped in a 2×2 complex matrix $\mathbf{V}$:

$$\mathbf{V}_{12}(u,v,\lambda) \equiv \left[\begin{array}{cc} V_{12,xx}(u,v,\lambda) & V_{12,xy}(u,v,\lambda) \\ V_{12,yx}(u,v,\lambda) & V_{12,yy}(u,v,\lambda) \end{array} \right]. \tag{1.13}$$

The sky brightness distribution I can also be written as a 2×2 matrix $\mathbf{B}$ using the Stokes parameters as a polarization basis:

$$\mathbf{B}_I(l,m,\lambda) \equiv \left[\begin{array}{cc} I(l,m,\lambda)+Q(l,m,\lambda) & U(l,m,\lambda)+iV(l,m,\lambda) \\ U(l,m,\lambda)-iV(l,m,\lambda) & I(l,m,\lambda)-Q(l,m,\lambda) \end{array} \right]. \tag{1.14}$$

At this point, equation 1.3 can be written by including the corruptions represented by the complex Jones matrices J: ([24],[60]):

$$\mathbf{V}_{12}(u,v,\lambda) = \mathbf{J}_1 \left(\int_\Omega \mathbf{B}_I(l,m,\lambda)\, e^{-2\pi i(ul+vm)} dl\, dm \right) \mathbf{J}_2^H \tag{1.15}$$

Equation 1.15 is known as the *measurement equation* and is the core of interferometric calibration. For an array with N antennas, equation 1.15 can be written for each of the $\frac{N(N-1)}{2}$ visibilities forming an overdetermined system of equations. The development of algorithms to solve the calibration system of equations is a very active research line ([38], [34], [66], [75], [63]) although beyond the scope of this chapter and we mention it here for completeness.

The solution of the measurement equation requires some knowledge of the sky brightness distribution $\mathbf{B}_I$, in other words, a *sky model*. Traditionally this is achieved by observing a calibration source, i.e. a bright, unresolved point source with known spectral and polarization properties. Calibration solutions are then applied to the observed field that is then used to improve the sky model $\mathbf{B}_I$ which, in turn, leads to more accurate calibration solutions $\mathbf{J}$. This loop that is traditionally called self calibration ([13], [50]) and can lead to a highly accurate calibration (e.g., [7], [61]).

The advantage of the measurement equation is that it can factorize different physical terms into different matrices. For example, the frequency response of the telescope electronics and its time variations essentially affects only the two polarization response and are modeled with a diagonal Jones matrix **B**:

$$\mathbf{B}(t,\lambda) \equiv \begin{bmatrix} b_x(t,\lambda) & 0 \\ 0 & b_y(t,\lambda) \end{bmatrix}, \tag{1.16}$$

where we made it explicit that **B** can vary with time and frequency. The undesired instrumental leakage between the two orthogonal polarized can be written as a **D** Jones matrix of the form:

$$\mathbf{D}(t,\lambda) \equiv \begin{bmatrix} 1 & d_x(t,\lambda) \\ -d_y(t,\nu) & 1 \end{bmatrix}, \tag{1.17}$$

and the measurement equation can be written as:

$$\mathbf{V}_{12}(u,v,\lambda) = \mathbf{B}_1\,\mathbf{D}_1 \left(\int_\Omega \mathbf{B}_I(l,m,\lambda)\, e^{-2\pi i(ul+vm)} dl\, dm \right) \mathbf{D}_2^H\, \mathbf{B}_2^H. \tag{1.18}$$

We note that, in principle, the primary beam response should appear as an additional 2×2 Jones matrix before the **D** matrix. For the purpose of this section we will neglect it, although we will illustrate an exception to this assumption when we later discuss about polarization calibration.

Retaining only the first order terms, equation 1.18 can be written as ([58]):

$$\begin{aligned}
V_{12,xx}(u,v,\lambda) &= b_{1,x} b^*_{2,x}[V_I(u,v,\lambda) - V_Q(u,v,\lambda)] &(1.19)\\
V_{12,xy}(u,v,\lambda) &= b_{1,x} b^*_{2,y}[(d_{1,x} - d^*_{2,y})V_I(u,v,\lambda) + V_U(u,v,\lambda) + iV_V(u,v,\lambda)] &(1.20)\\
V_{12,yx}(u,v,\lambda) &= b_{1,y} b^*_{2,x}[(d_{2,x} - d^*_{1,y})V_I(u,v,\lambda) + V_U(u,v,\lambda) - iV_V(u,v,\lambda)] &(1.21)\\
V_{12,yy}(u,v,\lambda) &= b_{1,y} b^*_{2,y}[V_I(u,v,\lambda) - V_Q(u,v,\lambda)], &(1.22)
\end{aligned}$$

where we dropped the explicit dependence on time and wavelength from the Jones matrices for notation clarity and where $V_{i=I,Q,U,V}$ are the Fourier transforms of the elements of the sky brightness matrix **B**.

This form of the measurement equation offers an intuitive understanding as to why calibration is of paramount important in 21 cm observations. The observed visibilities are essentially a measurement of foreground emission and, in the ideal case, their amplitudes would vary smoothly with frequency, allowing to avoid or subtract foregrounds. However, the instrumental response inevitably corrupts this smoothness in several ways: because the telescope primary beam is not sufficiently smooth in frequency, because of the electronic response or because of reflections along the signal path. Although calibration will correct for these effects and restore the intrinsic foreground frequency smoothness, calibration errors (i.e., deviations from the true **B** solutions) will still corrupt the foreground spectra. In practice, calibration errors result into foreground power leaking out of the horizon limit and jeopardizing (part of) the EoR window. The corruption of the foreground spectra will limit the accuracy of any subtraction method (see discussion in Chapter 6 in this book). *The effectiveness of foreground separation, proven in ideal cases, depends significantly on the accuracy of interferometric calibration.*

The form of the measurement equation written in equations 1.18 and 1.22 is often referred to as a *direction independent* calibration as it implicitly assumes that a single Jones matrix is sufficient to describe corruptions across the whole sky area of interest. This assumption is often invalid at low frequencies, mostly because of the changing primary beam response over a wide field of view, frequency, and the course of the observation, and the position and time dependent corruptions introduced by the Earth's ionosphere. In this case the measurement equation becomes *direction dependent*, i.e. a different Jones matrix is written and solved for a certain number of directions in the sky:

$$\mathbf{V}_{12}(u,v,\lambda) = \sum_s \left[\mathbf{B}_{1,s}\left(\int_\Omega \mathbf{B}_{I,s}(l,m,\lambda)\, e^{-2\pi i(ul+vm)} dl\, dm\right)\mathbf{B}^H_{2,s}\right], \quad (1.23)$$

where the sum is over the number of directions s. We note that we have used here the $\mathbf{B}$ matrix for pedagogical purposes, regardless of the physical origin of the direction dependent effect. Direction dependent effects also impact foreground separation, in a similar way as the direction independent effects.

Accurate direction independent and dependent calibration of 21 cm observations is a key topic of present research and can be grouped in a few main topics:

- *sky models*. Ideally, the sky brightness model matrix $\mathbf{B}_I$ (equation 1.18 and 1.22) would include the whole sky emission. This is pratically impossible as part of the sky signal is the unknown of interest (the 21 cm signal) and the detailed properties of the foreground sky are not known sufficiently well. Sky models are normally constituted of a catalogue of compact sources of known (or measured) properties, often covering an area significantly larger than the telescope field of view (e.g., [76], [52]). Nevertheless, sky models remain essentially always incomplete at some level, as source catalogues are limited in depth, source characterization and - often - sky coverage. [21], [74] and [22] show that incomplete catalogues used as sky models bias the calibration and eventually lead to artifacts in the form of ghost-like sources in interferometric images, most of the times fainter than the image noise level. The ghost pattern is stronger for regularly spaced arrays and if the sky model is less complete. In term of power spectrum, [19] and [4] show that the calibration bias introduced by incomplete sky models leads to an overall leakage of foreground power in the EoR window (Figure 1.3). A similar foreground leakage may occur because of the finite angular resolution of interferometric observations: for example, two sources whose size is respectively one third and one tenth of the instrument angular resolution will be both modeled as point like even if the first source is only barely unresolved. This biased catalogue would again lead to a leakage of foreground power in the EoR window ([54]). In this case, the bias can be mitigated by obtaining a sky model with an angular resolution much higher than the scales at which the 21 cm signal is expected ([54]).

  Sky models that include only compact sources are not adequate for baselines shorter than a few tens of meters as they are sensitive to Galactic diffuse emission, which contributes to most of the power on angular scales $\theta > 10-20$ arcmin (e.g., [6], [12]). Excluding short baselines from the calibration solutions prevents the problem of modeling diffuse emssion, but can bias the solutions ([49]) if the system of calibration equation is not properly regularized ([43]).

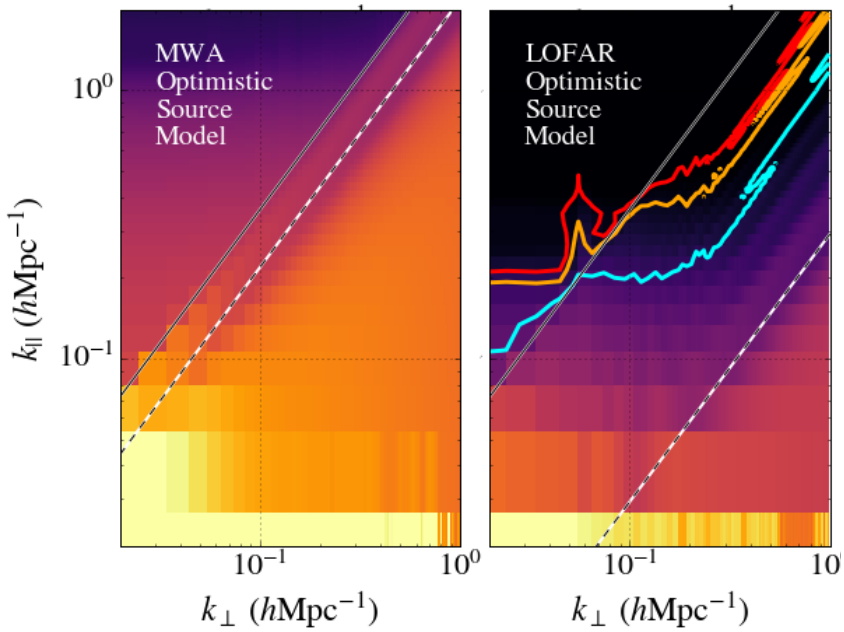

Figure 1.3: Example of power spectrum bias introduced by calibration errors due to an incomplete sky model for the Murchison Widefield Array (MWA, left) and the Low Frequency Array (LOFAR, right) cases respectively (from [19]). Power spectra are shown in their two dimensional $(k_{\perp}, k_{\parallel})$ form in order to display the foreground dominated region below the horizon limit (grey solid line). Cyan, orange and red lines are the locii where a fiducial 21 cm model power spectrum is one, five and ten times higher than the bias level. In an ideal case with perfectly smooth foregrounds and no calibration errors, the 21 cm power sepctrum should be detectable just outside the horizon limit. The errors introduced by an incomplete sky model leak foreground power in the EoR window at a level that may completely prevent a detection in the MWA case.

In summary, different analsysis approaches provide evidence that *imperfect sky models (either because of missing catalogue sources, mis-estimating source properties or missing diffuse emission) are a source of calibration bias that has general effect to corrupt the foreground properties, leaking their power well beyond the ideal horizon limit* and requiring additional modeling and subtraction. For this reason, significant efforts are currently ongoing in order to improve sky models via wider and deeper low frequency surveys (e.g., [26], [28], [59]), more accurate low frequency catalogues ([11]) and even better observations of Galactic diffuse emission ([78], [18]);

- *instrument/primary beam models*. A complete knowledge of a sky model may not be, by itself, sufficient for an accurate calibration of 21 cm observations as the brightness matrix $\mathbf{B}_I$ is multiplied by the antenna primary beam (equation 1.4 and 1.15) and the measurement of an intrinsic sky model requires the separation from the primary beam effect.

  Unlike steerable dishes, most 21 cm interferometers are constituted of dipoles fixed on the ground, in some cases clustered together to form larger stations whose beams that can be digitally pointed to a sky direction by introducing different delays to the dipoles (e.g., like the MWA and LOFAR arrays). As station beams are formed to track the source on the sky, the station projected area changes with time and the shape of the primay beam changes significantly (Figure 1.4). This is a typical direction dependent effect that can be casted in the measurement equation as

$$\mathbf{V}_{12}(u,v,\lambda) = \int_{\Omega} \mathbf{E}_1(t,l,m,\lambda)\mathbf{B}_{I,s}(l,m,\lambda)\, e^{-2\pi i(ul+vm)}\, \mathbf{E}_2^H(t,l,m,\lambda)dl\, dm, \quad (1.24)$$

  were $\mathbf{E}(t,l,m,\lambda)$ is the Jones matrix describing the primary beam which, in the simplest cases, is a diagonal matrix:

$$\mathbf{E}(t,l,m,\lambda) \equiv \begin{bmatrix} e_x(t,l,m,\lambda) & 0 \\ 0 & e_y(t,l,m,\lambda) \end{bmatrix}. \quad (1.25)$$

  We note that we have written the explicit dependence on the time due to change in projected area for dipole stations and that the direction dependence of the $\mathbf{E}$ is encoded in its (l,m) dependence.

  Time and frequency variable primary beams leads to apparent time variable sky models where variations that are larger away from the pointing direction due to the larger changes in the sidelobe pattern. For examples, sky sources that are well within the main lobe of the primary beam in Figure 1.4 will experience relatively negligible variations throughout an observation, the opposite will occur to sources located well outside the main lobe as they run through primary beam sidelobes.

  Primary beams are also frequency variable and, at first order, their size scales with wavelength (equation 1.2), i.e. rather smoothly. However, in the sidelobe region, variations become rather abrupt as the source can be located on a sidelobe peak at a certain frequency and in the sidelobe null at another frequency. As a final remark, stations that include several dipoles are not perfectly equal to each other, due to manifacturing reasons or mutual coupling between their elements (e.g., [64]), therefore $\mathbf{E}_1 \neq \mathbf{E}_2$. As primary beams are different, even visibilities for baselines that have the same length and orientation will be different - rather than identical, as expected. The left panel of Figure 1.4 shows an example of how much primary beams vary for different stations due to mutual coupling interactions: variations in the sidelobe region can be as large as $\sim 30\%$.

If not accurately modeled and taken into account, primary beam effects can bias the calibration solution and, again, corrupt the foreground frequency smoothness. [9], [65] and [67] have developed methods to incorporate time and frequency variable primary beams in interferometric images, however, the accuracy of the correction is limited by the accuracy of the primary beam model. Increasing effort is therefore being placed in precise modeling and measurements of the primary beams (e.g., [55], [16], [29], [15]);

- *polarization leakage calibration*. Equation 1.15 and 1.22 show that, even if the 21 cm signal is unpolarized, care needs to be taken against the contamination from polarized foreground emission. Most point sources are unpolarized below 200 MHz ([8], [35], [70]), therefore the assumption of an unpolarized sky model is well justified. However, calibration errors (in the matrix $\mathbf{B}$) would lead to a relative miscalibration of the xx and yy polarizations and, in turn, to leakage of polarized emission into total intensity. This effect may be particularly strong on short baselines (e.g., shorter than a ~ 1 km), where polarized foregrounds are brighter ([6], [27], [30], [35]). Polarized foregrounds that are Faraday rotated by the interstellar medium and leak to total intensity are a severe contamination to the 21 cm signal: they have a characteristic frequency dependence similar to the 21 cm signal therefore have power across the whole EoR window and cannot be subtracted using standard methods (e.g., [31], [39], [45]).

  Even if calibration errors are negligible, low frequency antennas have a non negligible polarized response across their wide field of view, i.e. the primary beam Jones matrix $\mathbf{E}$ is no longer diagonal. The measurement equation with a full polarized primary beam response can be written as ([45]):

$$\begin{aligned} \begin{bmatrix} V_{12,I}(u,v,\lambda) \\ V_{12,Q}(u,v,\lambda) \\ V_{12,U}(u,v,\lambda) \\ V_{12,V}(u,v,\lambda) \end{bmatrix} &= \int_{\Omega} \mathbf{S}^{-1}[\mathbf{E}_1 \otimes \mathbf{E}_2^H]\mathbf{S} \begin{bmatrix} I(l,m,\lambda) \\ Q(l,m,\lambda) \\ U(l,m,\lambda) \\ V(l,m,\lambda) \end{bmatrix} e^{-2\pi i(ul+vm)} dl\, dm = \\ &= \int_{\Omega} \mathbf{A}(l,m,\lambda) \begin{bmatrix} I(l,m,\lambda) \\ Q(l,m,\lambda) \\ U(l,m,\lambda) \\ V(l,m,\lambda) \end{bmatrix} e^{-2\pi i(ul+vm)} dl\, dm, \end{aligned} \tag{1.26}$$

  where $\mathbf{S}$ is the matrix that relates the intrisic Stokes parameters to the observer $x-y$ frame ([24]) and $\otimes$ is the outer product. Visibilities are written as a four-element vector as this form shows that the $\mathbf{A}$ matrix maps the intrinsic Stokes parameters into

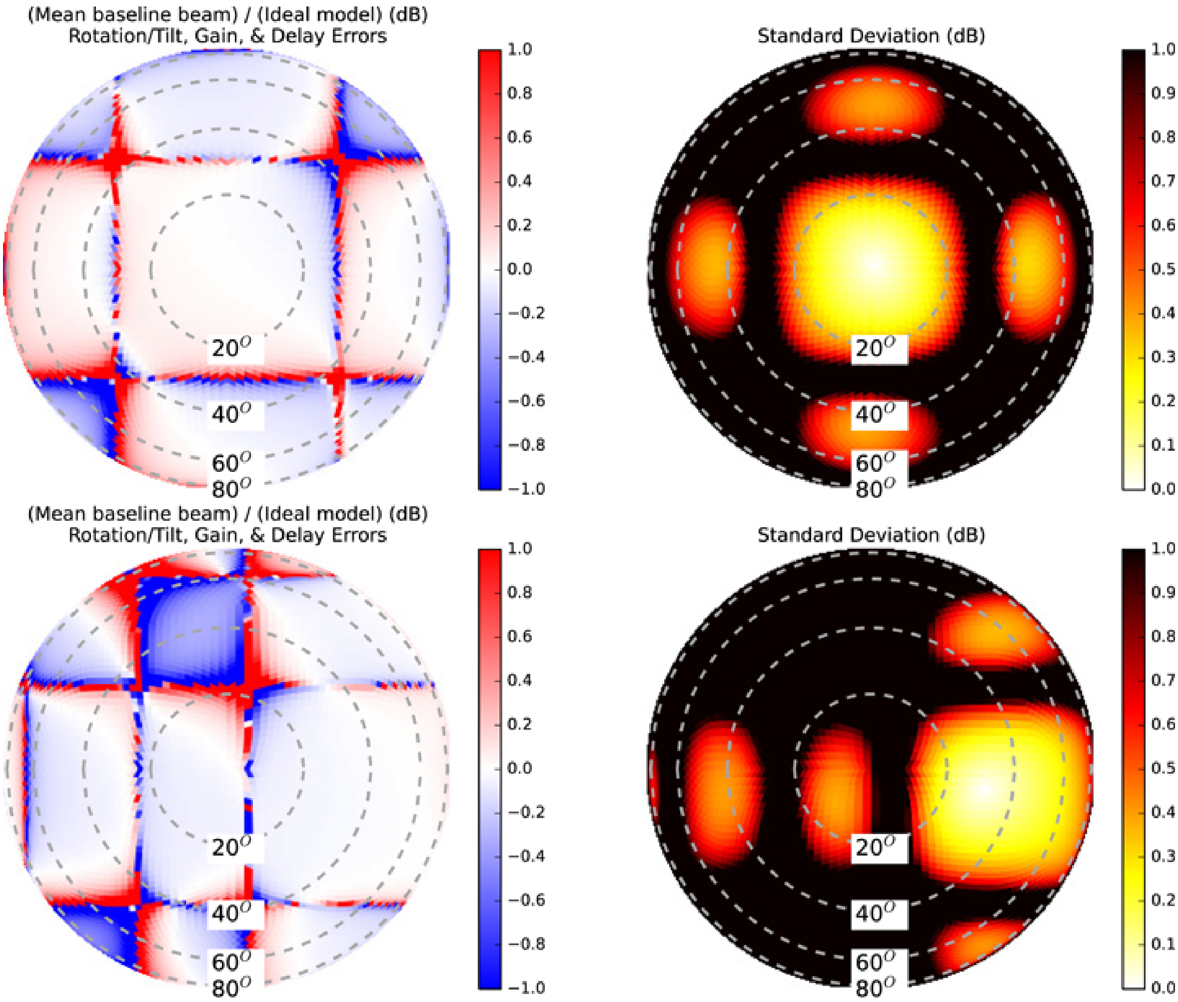

Figure 1.4: Example of primary beam variations as the MWA station points at zenith (top right) and $\sim 30^{\circ}$ away from zenith (bottom right) at 150 MHz. The left column shows the fractional variation of individual station beam models, with respect to the nominal primary beam (right column, from [44]. It is visibile how different the sidelobe pattern is when pointing towards two different directions. It should also be noticed the $\sim 10\%$ magnitude of the first lobe and the large null regions around the sidelobes. The specific pattern is due to the regular shape of the MWA station, where 16 dipoles are arrange in a square 4×4 grid.

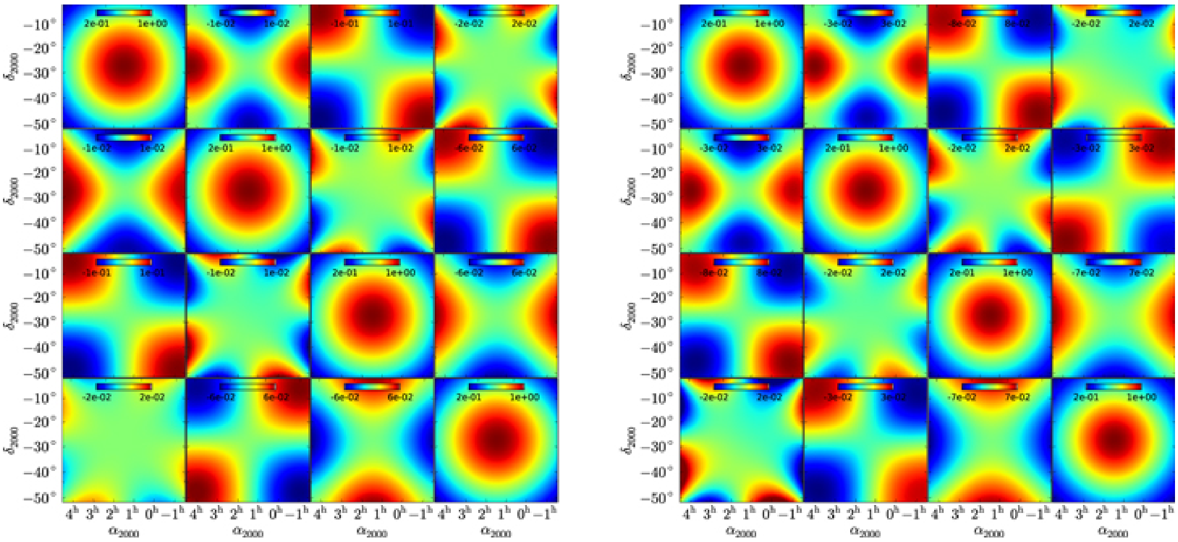

Figure 1.5: Examples of **A** matrices at 130 (left) and 150 MHz respectively (from [45]). The matrix maps the intrinsic Stokes parameters into observed ones: the diagonal terms represent the standard primary beam patterns, whereas the off-diagonal terms are the leakage terms. The second, the third and the fourth element of the first row show how Stokes parameters Q, U and V respectively contaminate the total intensity signal.

the observed ones:

$$\begin{pmatrix} I' \leftarrow I & I' \leftarrow Q & I' \leftarrow U & I' \leftarrow V \\ Q' \leftarrow I & Q' \leftarrow Q & Q' \leftarrow U & Q' \leftarrow V \\ U' \leftarrow I & U' \leftarrow Q & U' \leftarrow U & U' \leftarrow V \\ V' \leftarrow I & V' \leftarrow Q & V' \leftarrow U & V' \leftarrow V \end{pmatrix}. \tag{1.27}$$

An example of **A** matrix is shown in Figure 1.7. The first raw of the matrix shows how the four intrisinc Stokes parameters contribute to the observed total intensity and, therefore, how polarized foregrounds leak into the 21 cm signal even in absence of any calibration errors: the magnitude of the contaminating Stokes Q and U foregrounds increases away from the ponting direction. Wide-filed polarization is another textbook example of direction dependent calibration problem.

Calibration of polarization leakage remains a challenging task. Instruments with marrow fields of view naturally mitigate the leakege ([3], [2], [1]). It can also be mitigated by extending the sky model to include polarization (e.g. [20]), although modeling the diffuse Galactic foreground - the brightest component - is not straightforward and requires accurate imaging. However, [45] show that the magnitude of the Galactic polarization leakage may be below the 21 cm signal at high $k_\parallel$ values ($k > 0.3$ Mpc^{-1}) and, therefore, still be "avoided". A more extensive characterization of the polarized foreground properties is needed in order to extend their results to a general case.

- *ionospheric distortions*. The ionosphere is the partially ionized layer situated between ~ 50 and 1000 km above the surface of the Earth whose electron density changes

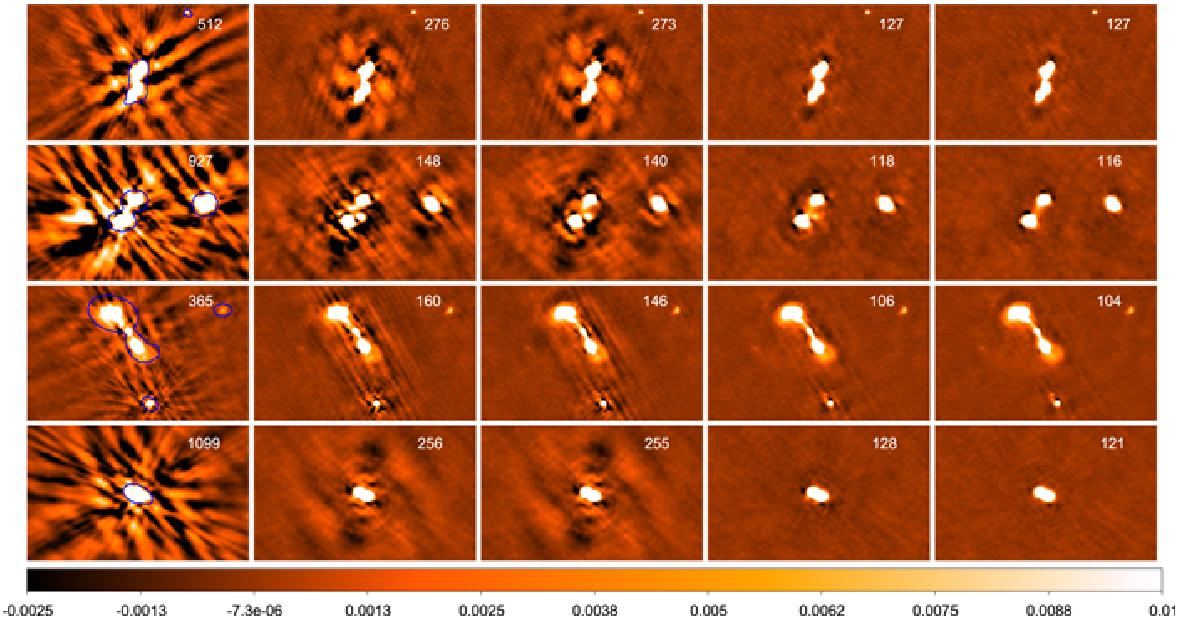

Figure 1.6: aaaaaaaaaaaaa.

with time and position. At low frequencies the ionosphere is no longer transparent to radio waves and scatters the incoming celestial wavefronts. The scattering magnitude depends upon the

1.3.1 Redundant calibration

An interferometric array where most of the baselines have the same length and orientation is called *redundant* as they measure the same Fourier mode of the sky brightness distribution. Redundant array configurations are often not appealing as they have poor imaging performances as they do not measure sufficient Fourier modes to reconstruct accurate sky images. However, a maximally redundant array where the antennas are laid out in a regularly spaced square grid offers the maximum power spectrum sensitivity on the $k_\perp$ modes corresponding to the most numerous baselines. This criterium has inspired the highly redundant layouts of the MIT Epoch of Reionization experiment ([77]), the Precision Array to Probe the Epoch of Reionization (PAPER, [46]) and partly driven the updated MWA.

One of the advantages of a redundant array is that it enables a different calibration strategy called *redundant calibration*. In redundant calibration the form of the measurement equation does not change and can be written, for a single polarization, like equation 1.22:

$$V_{12,xx}(u,v,\lambda) = b_{1,x} b^*_{2,x} y_{12,xx}(u,v,\lambda), \tag{1.28}$$

with the difference now that the model visibility y is not tied to a sky model, but it is solved for, simply assuming that it is the same for each group of redundant baselines [73], [36]). In other words, redundant calibration is independent on the sky model and, therefore, bypasses entirely the biases related to sky model incompleteness described in Section 1.3. However, as redundant calibration is not tied to any physical (i.e. sky-based) spatial or spectral model,

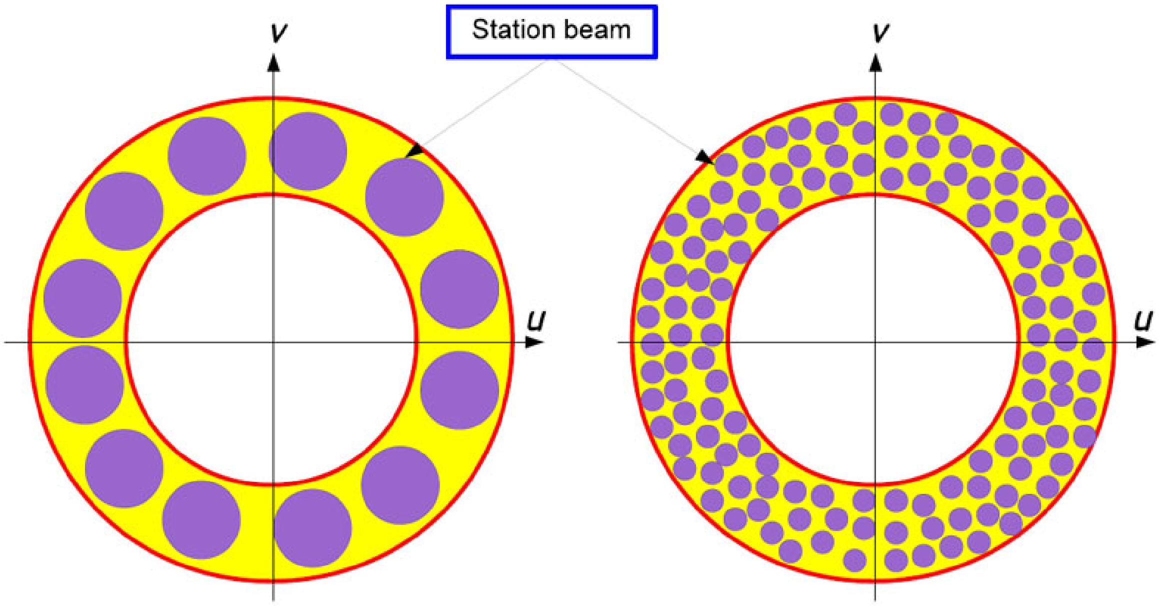

Figure 1.7: Cartoon illustration of the *uv* footprint due to the primary beam.

its solutions have degeneracies that need to be solved for by using a sky model (e.g., [77], [10]). In particular, spectral calibration, which is critical for foreground separation, cannot currently be obtained using redundant calibration and requires a sky-based calibration. [10] suggest that sky model incompleteness can bias this calibration step, in a way similar to what happens with a traditional calibration scheme.

Redundant calibration is also prone to effects that break the assumption of redundancy, the most common being errors in the antenna positions and different primary beams for different antennas. Even if antenna position errors can be reduced to have a negligible impact on redundant calibration [32], the effect of primary beam variations amongts the different antennas on redundant calibration is still largely unknown. **Comment on the limitations of redundant calibration to treat polarization.**

1.4 Array design and observing strategies

I will conclude this chapter by discussing how the various interferometric effects discussed so far impact the choice of array designs and the consequent observing strategies. [40] and [46], for example, investigate how instrumental choices like the array layout, the antenna size and the bandwidth (do not) affect the 21 cm power spectrum spectrum. Here I would rather like to emphasize the interdependence between instrumental choices and calibration and foreground separation strategies. If the total collecting area is kept fixed, there are two main elements that impact calibration and foreground separation:

- *station size*. The choice of station size determines the minimum $k_\perp$ value accessible and the footprint of each *uv* measurement. Indeed each visibility is not a single point in the *uv* plane but has a footprint corresponding to the two dimensional Fourier transform of the primary beam. This can be seen using the convolution theorem to re-write equation 1.1:

$$V_{ij}(\mathbf{b},\lambda) = \tilde{A}(\mathbf{b},\lambda) * \tilde{I}(\mathbf{b},\lambda). \tag{1.29}$$

- *array layout* Beyond the obvious sensitivity requirement, decisions need to be taken as to which layout to adopt, which antenna size and these choice are intrinsically related to calibration and foreground separation strategies. For instance a filled *uv*-coverage (between the minimum and the maximum station separation) is highly desirable for imaging, modeling and subtracting foregrounds. It is not a stringent requirement for power spectrum measurement and in the avoidance strategy.

As examples, I will use four existing low frequency arrays that, concidentally, span the range of parameters of interest:

- effect of the field of view, calibratability, uv cell, drift scan versus tracking, suppression of sources outside the main lobe ionosphere
- uv coverage choices power spectra vs images, redundant vs pseud random (reconstructing sky brightness), minimum/maximum k mode accessible... avoidance (compact) vs subtraction (less compact)
- obviously sensitivity
- *Low Frequency Array (LOFAR)*. LOFAR is an array mainly located in The Nerthelands but it include also remote stations acroos Europe. Each station
- Murchison Widefield Array (MWA)
- Precision Array to Probe the Epoch of Reionization (PAPER)
- Hydrogen Epoch of Reionization Array (HERA)
- Square Kilomtre Array (SKA)

Bibliography

[1] K. M. B. Asad, L. V. E. Koopmans, V. Jelić, A. G. de Bruyn, V. N. Pandey, and B. K. Gehlot. Polarization leakage in epoch of reionization windows - III. Wide-field effects of narrow-field arrays. *MNRAS*, 476:3051–3062, May 2018.

[2] K. M. B. Asad, L. V. E. Koopmans, V. Jelić, A. Ghosh, F. B. Abdalla, M. A. Brentjens, A. G. de Bruyn, B. Ciardi, B. K. Gehlot, I. T. Iliev, M. Mevius, V. N. Pandey, S. Yatawatta, and S. Zaroubi. Polarization leakage in epoch of reionization windows - II. Primary beam model and direction-dependent calibration. *MNRAS*, 462:4482–4494, November 2016.

[3] K. M. B. Asad, L. V. E. Koopmans, V. Jelić, V. N. Pandey, A. Ghosh, F. B. Abdalla, G. Bernardi, M. A. Brentjens, A. G. de Bruyn, S. Bus, B. Ciardi, E. Chapman, S. Daiboo, E. R. Fernandez, G. Harker, I. T. Iliev, H. Jensen, O. Martinez-Rubi, G. Mellema, M. Mevius, A. R. Offringa, A. H. Patil, J. Schaye, R. M. Thomas, S. van der Tol, H. K. Vedantham, S. Yatawatta, and S. Zaroubi. Polarization leakage in epoch of reionization windows - I. Low Frequency Array observations of the 3C196 field. *MNRAS*, 451:3709–3727, August 2015.

[4] N. Barry, B. Hazelton, I. Sullivan, M. F. Morales, and J. C. Pober. Calibration requirements for detecting the 21 cm epoch of reionization power spectrum and implications for the SKA. *MNRAS*, 461:3135–3144, September 2016.

[5] A. P. Beardsley, B. J. Hazelton, I. S. Sullivan, P. Carroll, N. Barry, M. Rahimi, B. Pindor, C. M. Trott, J. Line, D. C. Jacobs, M. F. Morales, J. C. Pober, G. Bernardi, J. D. Bowman, M. P. Busch, F. Briggs, R. J. Cappallo, B. E. Corey, A. de Oliveira-Costa, J. S. Dillon, D. Emrich, A. Ewall-Wice, L. Feng, B. M. Gaensler, R. Goeke, L. J. Greenhill, J. N. Hewitt, N. Hurley-Walker, M. Johnston-Hollitt, D. L. Kaplan, J. C. Kasper, H. S. Kim, E. Kratzenberg, E. Lenc, A. Loeb, C. J. Lonsdale, M. J. Lynch, B. McKinley, S. R. McWhirter, D. A. Mitchell, E. Morgan, A. R. Neben, N. Thyagarajan, D. Oberoi, A. R. Offringa, S. M. Ord, S. Paul, T. Prabu, P. Procopio, J. Riding, A. E. E. Rogers, A. Roshi, N. Udaya Shankar, S. K. Sethi, K. S. Srivani, R. Subrahmanyan, M. Tegmark, S. J. Tingay, M. Waterson, R. B. Wayth, R. L. Webster, A. R. Whitney, A. Williams, C. L. Williams, C. Wu, and J. S. B. Wyithe. First Season MWA EoR Power spectrum Results at Redshift 7. *ApJ*, 833:102, December 2016.

[6] G. Bernardi, A. G. de Bruyn, M. A. Brentjens, B. Ciardi, G. Harker, V. Jelić, L. V. E. Koopmans, P. Labropoulos, A. Offringa, V. N. Pandey, J. Schaye, R. M. Thomas,

S. Yatawatta, and S. Zaroubi. Foregrounds for observations of the cosmological 21 cm line. I. First Westerbork measurements of Galactic emission at 150 MHz in a low latitude field. *A&A*, 500:965–979, June 2009.

[7] G. Bernardi, A. G. de Bruyn, G. Harker, M. A. Brentjens, B. Ciardi, V. Jelić, L. V. E. Koopmans, P. Labropoulos, A. Offringa, V. N. Pandey, J. Schaye, R. M. Thomas, S. Yatawatta, and S. Zaroubi. Foregrounds for observations of the cosmological 21 cm line. II. Westerbork observations of the fields around 3C 196 and the North Celestial Pole. *A&A*, 522:A67, November 2010.

[8] G. Bernardi, L. J. Greenhill, D. A. Mitchell, S. M. Ord, B. J. Hazelton, B. M. Gaensler, A. de Oliveira-Costa, M. F. Morales, N. Udaya Shankar, R. Subrahmanyan, R. B. Wayth, E. Lenc, C. L. Williams, W. Arcus, B. S. Arora, D. G. Barnes, J. D. Bowman, F. H. Briggs, J. D. Bunton, R. J. Cappallo, B. E. Corey, A. Deshpande, L. deSouza, D. Emrich, R. Goeke, D. Herne, J. N. Hewitt, M. Johnston-Hollitt, D. Kaplan, J. C. Kasper, B. B. Kincaid, R. Koenig, E. Kratzenberg, C. J. Lonsdale, M. J. Lynch, S. R. McWhirter, E. Morgan, D. Oberoi, J. Pathikulangara, T. Prabu, R. A. Remillard, A. E. E. Rogers, A. Roshi, J. E. Salah, R. J. Sault, K. S. Srivani, J. Stevens, S. J. Tingay, M. Waterson, R. L. Webster, A. R. Whitney, A. Williams, and J. S. B. Wyithe. A 189 MHz, 2400 deg^2 Polarization Survey with the Murchison Widefield Array 32-element Prototype. *ApJ*, 771:105, July 2013.

[9] S. Bhatnagar, T. J. Cornwell, K. Golap, and J. M. Uson. Correcting direction-dependent gains in the deconvolution of radio interferometric images. *A&A*, 487:419–429, August 2008.

[10] R. Byrne, M. F. Morales, B. Hazelton, W. Li, N. Barry, A. P. Beardsley, R. Joseph, J. Pober, I. Sullivan, and C. Trott. Fundamental Limitations on the Calibration of Redundant 21 cm Cosmology Instruments and Implications for HERA and the SKA. *ApJ*, 875:70, April 2019.

[11] P. A. Carroll, J. Line, M. F. Morales, N. Barry, A. P. Beardsley, B. J. Hazelton, D. C. Jacobs, J. C. Pober, I. S. Sullivan, R. L. Webster, G. Bernardi, J. D. Bowman, F. Briggs, R. J. Cappallo, B. E. Corey, A. de Oliveira-Costa, J. S. Dillon, D. Emrich, A. Ewall-Wice, L. Feng, B. M. Gaensler, R. Goeke, L. J. Greenhill, J. N. Hewitt, N. Hurley-Walker, M. Johnston-Hollitt, D. L. Kaplan, J. C. Kasper, H. Kim, E. Kratzenberg, E. Lenc, A. Loeb, C. J. Lonsdale, M. J. Lynch, B. McKinley, S. R. McWhirter, D. A. Mitchell, E. Morgan, A. R. Neben, D. Oberoi, A. R. Offringa, S. M. Ord, S. Paul, B. Pindor, T. Prabu, P. Procopio, J. Riding, A. E. E. Rogers, A. Roshi, N. U. Shankar, S. K. Sethi, K. S. Srivani, R. Subrahmanyan, M. Tegmark, N. Thyagarajan, S. J. Tingay, C. M. Trott, M. Waterson, R. B. Wayth, A. R. Whitney, A. Williams, C. L. Williams, C. Wu, and J. S. B. Wyithe. A high reliability survey of discrete Epoch of Reionization foreground sources in the MWA EoR0 field. *MNRAS*, 461:4151–4175, October 2016.

[12] S. Choudhuri, S. Bharadwaj, S. S. Ali, N. Roy, H. T. Intema, and A. Ghosh. The angular power spectrum measurement of the Galactic synchrotron emission in two fields of the TGSS survey. *MNRAS*, 470:L11–L15, September 2017.

[13] T. J. Cornwell and P. N. Wilkinson. A new method for making maps with unstable radio interferometers. *MNRAS*, 196:1067–1086, September 1981.

[14] K. K. Datta, M. M. Friedrich, G. Mellema, I. T. Iliev, and P. R. Shapiro. Prospects of observing a quasar H II region during the epoch of reionization with the redshifted 21-cm signal. *MNRAS*, 424:762–778, July 2012.

[15] E. de Lera Acedo, P. Bolli, F. Paonessa, G. Virone, E. Colin-Beltran, N. Razavi-Ghods, I. Aicardi, A. Lingua, P. Maschio, J. Monari, G. Naldi, M. Piras, and G. Pupillo. SKA aperture array verification system: electromagnetic modeling and beam pattern measurements using a micro UAV. *Experimental Astronomy*, 45:1–20, March 2018.

[16] E. de Lera Acedo, C. M. Trott, R. B. Wayth, N. Fagnoni, G. Bernardi, B. Wakley, L. V. E. Koopmans, A. J. Faulkner, and J. G. bij de Vaate. Spectral performance of SKA Log-periodic Antennas I: mitigating spectral artefacts in SKA1-LOW 21 cm cosmology experiments. *MNRAS*, 469:2662–2671, August 2017.

[17] C. Dickinson, R. A. Battye, P. Carreira, K. Cleary, R. D. Davies, R. J. Davis, R. Genova-Santos, K. Grainge, C. M. Gutiérrez, Y. A. Hafez, M. P. Hobson, M. E. Jones, R. Kneissl, K. Lancaster, A. Lasenby, J. P. Leahy, K. Maisinger, C. Ödman, G. Pooley, N. Rajguru, R. Rebolo, J. A. Rubiño-Martin, R. D. E. Saunders, R. S. Savage, A. Scaife, P. F. Scott, A. Slosar, P. Sosa Molina, A. C. Taylor, D. Titterington, E. Waldram, R. A. Watson, and A. Wilkinson. High-sensitivity measurements of the cosmic microwave background power spectrum with the extended Very Small Array. *MNRAS*, 353:732–746, September 2004.

[18] J. Dowell, G. B. Taylor, F. K. Schinzel, N. E. Kassim, and K. Stovall. The LWA1 Low Frequency Sky Survey. *MNRAS*, 469:4537–4550, August 2017.

[19] A. Ewall-Wice, J. S. Dillon, A. Liu, and J. Hewitt. The impact of modelling errors on interferometer calibration for 21 cm power spectra. *MNRAS*, 470:1849–1870, September 2017.

[20] P. M. Geil, B. M. Gaensler, and J. S. B. Wyithe. Polarized foreground removal at low radio frequencies using rotation measure synthesis: uncovering the signature of hydrogen reionization. *MNRAS*, 418:516–535, November 2011.

[21] T. L. Grobler, C. D. Nunhokee, O. M. Smirnov, A. J. van Zyl, and A. G. de Bruyn. Calibration artefacts in radio interferometry - I. Ghost sources in Westerbork Synthesis Radio Telescope data. *MNRAS*, 439:4030–4047, April 2014.

[22] T. L. Grobler, A. J. Stewart, S. J. Wijnholds, J. S. Kenyon, and O. M. Smirnov. Calibration artefacts in radio interferometry - III. Phase-only calibration and primary beam correction. *MNRAS*, 461:2975–2992, September 2016.

[23] N. W. Halverson, E. M. Leitch, C. Pryke, J. Kovac, J. E. Carlstrom, W. L. Holzapfel, M. Dragovan, J. K. Cartwright, B. S. Mason, S. Padin, T. J. Pearson, A. C. S. Readhead, and M. C. Shepherd. Degree Angular Scale Interferometer First Results: A

Measurement of the Cosmic Microwave Background Angular Power Spectrum. *ApJ*, 568:38–45, March 2002.

[24] J. P. Hamaker, J. D. Bregman, and R. J. Sault. Understanding radio polarimetry. I. Mathematical foundations. *A&AS*, 117:137–147, May 1996.

[25] G. Harker, S. Zaroubi, G. Bernardi, M. A. Brentjens, A. G. de Bruyn, B. Ciardi, V. Jelić, L. V. E. Koopmans, P. Labropoulos, G. Mellema, A. Offringa, V. N. Pandey, A. H. Pawlik, J. Schaye, R. M. Thomas, and S. Yatawatta. Power spectrum extraction for redshifted 21-cm Epoch of Reionization experiments: the LOFAR case. *MNRAS*, 405:2492–2504, July 2010.

[26] N. Hurley-Walker, J. R. Callingham, P. J. Hancock, T. M. O. Franzen, L. Hindson, A. D. Kapińska, J. Morgan, A. R. Offringa, R. B. Wayth, C. Wu, Q. Zheng, T. Murphy, M. E. Bell, K. S. Dwarakanath, B. For, B. M. Gaensler, M. Johnston-Hollitt, E. Lenc, P. Procopio, L. Staveley-Smith, R. Ekers, J. D. Bowman, F. Briggs, R. J. Cappallo, A. A. Deshpande, L. Greenhill, B. J. Hazelton, D. L. Kaplan, C. J. Lonsdale, S. R. McWhirter, D. A. Mitchell, M. F. Morales, E. Morgan, D. Oberoi, S. M. Ord, T. Prabu, N. U. Shankar, K. S. Srivani, R. Subrahmanyan, S. J. Tingay, R. L. Webster, A. Williams, and C. L. Williams. GaLactic and Extragalactic All-sky Murchison Widefield Array (GLEAM) survey - I. A low-frequency extragalactic catalogue. *MNRAS*, 464:1146–1167, January 2017.

[27] M. Iacobelli, M. Haverkorn, E. Orrú, R. F. Pizzo, J. Anderson, R. Beck, M. R. Bell, A. Bonafede, K. Chyzy, R.-J. Dettmar, T. A. Enßlin, G. Heald, C. Horellou, A. Horneffer, W. Jurusik, H. Junklewitz, M. Kuniyoshi, D. D. Mulcahy, R. Paladino, W. Reich, A. Scaife, C. Sobey, C. Sotomayor-Beltran, A. Alexov, A. Asgekar, I. M. Avruch, M. E. Bell, I. van Bemmel, M. J. Bentum, G. Bernardi, P. Best, L. Bırzan, F. Breitling, J. Broderick, W. N. Brouw, M. Brüggen, H. R. Butcher, B. Ciardi, J. E. Conway, F. de Gasperin, E. de Geus, S. Duscha, J. Eislöffel, D. Engels, H. Falcke, R. A. Fallows, C. Ferrari, W. Frieswijk, M. A. Garrett, J. Grießmeier, A. W. Gunst, J. P. Hamaker, T. E. Hassall, J. W. T. Hessels, M. Hoeft, J. Hörandel, V. Jelic, A. Karastergiou, V. I. Kondratiev, L. V. E. Koopmans, M. Kramer, G. Kuper, J. van Leeuwen, G. Macario, G. Mann, J. P. McKean, H. Munk, M. Pandey-Pommier, A. G. Polatidis, H. Röttgering, D. Schwarz, J. Sluman, O. Smirnov, B. W. Stappers, M. Steinmetz, M. Tagger, Y. Tang, C. Tasse, C. Toribio, R. Vermeulen, C. Vocks, C. Vogt, R. J. van Weeren, M. W. Wise, O. Wucknitz, S. Yatawatta, P. Zarka, and A. Zensus. Studying Galactic interstellar turbulence through fluctuations in synchrotron emission. First LOFAR Galactic foreground detection. *A&A*, 558:A72, October 2013.

[28] H. T. Intema, P. Jagannathan, K. P. Mooley, and D. A. Frail. The GMRT 150 MHz all-sky radio survey. First alternative data release TGSS ADR1. *A&A*, 598:A78, February 2017.

[29] D. C. Jacobs, J. Burba, J. D. Bowman, A. R. Neben, B. Stinnett, L. Turner, K. Johnson, M. Busch, J. Allison, M. Leatham, V. Serrano Rodriguez, M. Denney, and D. Nel-

son. First Demonstration of ECHO: an External Calibrator for Hydrogen Observatories. *PASP*, 129(3):035002, March 2017.

[30] V. Jelić, A. G. de Bruyn, V. N. Pandey, M. Mevius, M. Haverkorn, M. A. Brentjens, L. V. E. Koopmans, S. Zaroubi, F. B. Abdalla, K. M. B. Asad, S. Bus, E. Chapman, B. Ciardi, E. R. Fernandez, A. Ghosh, G. Harker, I. T. Iliev, H. Jensen, S. Kazemi, G. Mellema, A. R. Offringa, A. H. Patil, H. K. Vedantham, and S. Yatawatta. Linear polarization structures in LOFAR observations of the interstellar medium in the 3C 196 field. *A&A*, 583:A137, November 2015.

[31] V. Jelić, S. Zaroubi, P. Labropoulos, G. Bernardi, A. G. de Bruyn, and L. V. E. Koopmans. Realistic simulations of the Galactic polarized foreground: consequences for 21-cm reionization detection experiments. *MNRAS*, 409:1647–1659, December 2010.

[32] R. C. Joseph, C. M. Trott, and R. B. Wayth. The Bias and Uncertainty of Redundant and Sky-based Calibration Under Realistic Sky and Telescope Conditions. *AJ*, 156:285, December 2018.

[33] K. Kakiichi, S. Majumdar, G. Mellema, B. Ciardi, K. L. Dixon, I. T. Iliev, V. Jelić, L. V. E. Koopmans, S. Zaroubi, and P. Busch. Recovering the H II region size statistics from 21-cm tomography. *MNRAS*, 471:1936–1954, October 2017.

[34] S. Kazemi, S. Yatawatta, S. Zaroubi, P. Lampropoulos, A. G. de Bruyn, L. V. E. Koopmans, and J. Noordam. Radio interferometric calibration using the SAGE algorithm. *MNRAS*, 414:1656–1666, June 2011.

[35] E. Lenc, B. M. Gaensler, X. H. Sun, E. M. Sadler, A. G. Willis, N. Barry, A. P. Beardsley, M. E. Bell, G. Bernardi, J. D. Bowman, F. Briggs, J. R. Callingham, R. J. Cappallo, P. Carroll, B. E. Corey, A. de Oliveira-Costa, A. A. Deshpande, J. S. Dillon, K. S. Dwarkanath, D. Emrich, A. Ewall-Wice, L. Feng, B.-Q. For, R. Goeke, L. J. Greenhill, P. Hancock, B. J. Hazelton, J. N. Hewitt, L. Hindson, N. Hurley-Walker, M. Johnston-Hollitt, D. C. Jacobs, A. D. Kapińska, D. L. Kaplan, J. C. Kasper, H.-S. Kim, E. Kratzenberg, J. Line, A. Loeb, C. J. Lonsdale, M. J. Lynch, B. McKinley, S. R. McWhirter, D. A. Mitchell, M. F. Morales, E. Morgan, J. Morgan, T. Murphy, A. R. Neben, D. Oberoi, A. R. Offringa, S. M. Ord, S. Paul, B. Pindor, J. C. Pober, T. Prabu, P. Procopio, J. Riding, A. E. E. Rogers, A. Roshi, N. Udaya Shankar, S. K. Sethi, K. S. Srivani, L. Staveley-Smith, R. Subrahmanyan, I. S. Sullivan, M. Tegmark, N. Thyagarajan, S. J. Tingay, C. Trott, M. Waterson, R. B. Wayth, R. L. Webster, A. R. Whitney, A. Williams, C. L. Williams, C. Wu, J. S. B. Wyithe, and Q. Zheng. Low-frequency Observations of Linearly Polarized Structures in the Interstellar Medium near the South Galactic Pole. *ApJ*, 830:38, October 2016.

[36] A. Liu, M. Tegmark, S. Morrison, A. Lutomirski, and M. Zaldarriaga. Precision calibration of radio interferometers using redundant baselines. *MNRAS*, 408:1029–1050, October 2010.

[37] G. Mellema, L. V. E. Koopmans, F. A. Abdalla, G. Bernardi, B. Ciardi, S. Daiboo, A. G. de Bruyn, K. K. Datta, H. Falcke, A. Ferrara, I. T. Iliev, F. Iocco, V. Jelić, H. Jensen,

R. Joseph, P. Labroupoulos, A. Meiksin, A. Mesinger, A. R. Offringa, V. N. Pandey, J. R. Pritchard, M. G. Santos, D. J. Schwarz, B. Semelin, H. Vedantham, S. Yatawatta, and S. Zaroubi. Reionization and the Cosmic Dawn with the Square Kilometre Array. *Experimental Astronomy*, 36:235–318, August 2013.

[38] D. A. Mitchell, L. J. Greenhill, R. B. Wayth, R. J. Sault, C. J. Lonsdale, R. J. Cappallo, M. F. Morales, and S. M. Ord. Real-Time Calibration of the Murchison Widefield Array. *IEEE Journal of Selected Topics in Signal Processing*, 2:707–717, November 2008.

[39] D. F. Moore, J. E. Aguirre, A. R. Parsons, D. C. Jacobs, and J. C. Pober. The Effects of Polarized Foregrounds on 21 cm Epoch of Reionization Power Spectrum Measurements. *ApJ*, 769:154, June 2013.

[40] M. F. Morales. Power Spectrum Sensitivity and the Design of Epoch of Reionization Observatories. *ApJ*, 619:678–683, February 2005.

[41] M. F. Morales, B. Hazelton, I. Sullivan, and A. Beardsley. Four Fundamental Foreground Power Spectrum Shapes for 21 cm Cosmology Observations. *ApJ*, 752:137, June 2012.

[42] M. F. Morales and J. Hewitt. Toward Epoch of Reionization Measurements with Wide-Field Radio Observations. *ApJ*, 615:7–18, November 2004.

[43] A. Mouri Sardarabadi and L. V. E. Koopmans. Quantifying suppression of the cosmological 21-cm signal due to direction-dependent gain calibration in radio interferometers. *MNRAS*, 483:5480–5490, March 2019.

[44] A. R. Neben, J. N. Hewitt, R. F. Bradley, J. S. Dillon, G. Bernardi, J. D. Bowman, F. Briggs, R. J. Cappallo, B. E. Corey, A. A. Deshpande, R. Goeke, L. J. Greenhill, B. J. Hazelton, M. Johnston-Hollitt, D. L. Kaplan, C. J. Lonsdale, S. R. McWhirter, D. A. Mitchell, M. F. Morales, E. Morgan, D. Oberoi, S. M. Ord, T. Prabu, N. Udaya Shankar, K. S. Srivani, R. Subrahmanyan, S. J. Tingay, R. B. Wayth, R. L. Webster, A. Williams, and C. L. Williams. Beam-forming Errors in Murchison Widefield Array Phased Array Antennas and their Effects on Epoch of Reionization Science. *ApJ*, 820:44, March 2016.

[45] C. D. Nunhokee, G. Bernardi, S. A. Kohn, J. E. Aguirre, N. Thyagarajan, J. S. Dillon, G. Foster, T. L. Grobler, J. Z. E. Martinot, and A. R. Parsons. Constraining Polarized Foregrounds for EoR Experiments. II. Polarization Leakage Simulations in the Avoidance Scheme. *ApJ*, 848:47, October 2017.

[46] A. Parsons, J. Pober, M. McQuinn, D. Jacobs, and J. Aguirre. A Sensitivity and Array-configuration Study for Measuring the Power Spectrum of 21 cm Emission from Reionization. *ApJ*, 753:81, July 2012.

[47] A. R. Parsons, J. C. Pober, J. E. Aguirre, C. L. Carilli, D. C. Jacobs, and D. F. Moore. A Per-baseline, Delay-spectrum Technique for Accessing the 21 cm Cosmic Reionization Signature. *ApJ*, 756:165, September 2012.

[48] A. H. Patil, S. Yatawatta, L. V. E. Koopmans, A. G. de Bruyn, M. A. Brentjens, S. Zaroubi, K. M. B. Asad, M. Hatef, V. Jelić, M. Mevius, A. R. Offringa, V. N. Pandey, H. Vedantham, F. B. Abdalla, W. N. Brouw, E. Chapman, B. Ciardi, B. K. Gehlot, A. Ghosh, G. Harker, I. T. Iliev, K. Kakiichi, S. Majumdar, G. Mellema, M. B. Silva, J. Schaye, D. Vrbanec, and S. J. Wijnholds. Upper Limits on the 21 cm Epoch of Reionization Power Spectrum from One Night with LOFAR. *ApJ*, 838:65, March 2017.

[49] A. H. Patil, S. Yatawatta, S. Zaroubi, L. V. E. Koopmans, A. G. de Bruyn, V. Jelić, B. Ciardi, I. T. Iliev, M. Mevius, V. N. Pandey, and B. K. Gehlot. Systematic biases in low-frequency radio interferometric data due to calibration: the LOFAR-EoR case. *MNRAS*, 463:4317–4330, December 2016.

[50] T. J. Pearson and A. C. S. Readhead. Image Formation by Self-Calibration in Radio Astronomy. *ARAA*, 22:97–130, 1984.

[51] U.-L. Pen, T.-C. Chang, C. M. Hirata, J. B. Peterson, J. Roy, Y. Gupta, J. Odegova, and K. Sigurdson. The GMRT EoR experiment: limits on polarized sky brightness at 150 MHz. *MNRAS*, 399:181–194, October 2009.

[52] J. C. Pober, B. J. Hazelton, A. P. Beardsley, N. A. Barry, Z. E. Martinot, I. S. Sullivan, M. F. Morales, M. E. Bell, G. Bernardi, N. D. R. Bhat, J. D. Bowman, F. Briggs, R. J. Cappallo, P. Carroll, B. E. Corey, A. de Oliveira-Costa, A. A. Deshpande, J. S. Dillon, D. Emrich, A. M. Ewall-Wice, L. Feng, R. Goeke, L. J. Greenhill, J. N. Hewitt, L. Hindson, N. Hurley-Walker, D. C. Jacobs, M. Johnston-Hollitt, D. L. Kaplan, J. C. Kasper, H.-S. Kim, P. Kittiwisit, E. Kratzenberg, N. Kudryavtseva, E. Lenc, J. Line, A. Loeb, C. J. Lonsdale, M. J. Lynch, B. McKinley, S. R. McWhirter, D. A. Mitchell, E. Morgan, A. R. Neben, D. Oberoi, A. R. Offringa, S. M. Ord, S. Paul, B. Pindor, T. Prabu, P. Procopio, J. Riding, A. E. E. Rogers, A. Roshi, S. K. Sethi, N. Udaya Shankar, K. S. Srivani, R. Subrahmanyan, M. Tegmark, N. Thyagarajan, S. J. Tingay, C. M. Trott, M. Waterson, R. B. Wayth, R. L. Webster, A. R. Whitney, A. Williams, C. L. Williams, and J. S. B. Wyithe. The Importance of Wide-field Foreground Removal for 21 cm Cosmology: A Demonstration with Early MWA Epoch of Reionization Observations. *ApJ*, 819:8, March 2016.

[53] J. C. Pober, A. R. Parsons, J. E. Aguirre, Z. Ali, R. F. Bradley, C. L. Carilli, D. DeBoer, M. Dexter, N. E. Gugliucci, D. C. Jacobs, P. J. Klima, D. MacMahon, J. Manley, D. F. Moore, I. I. Stefan, and W. P. Walbrugh. Opening the 21 cm Epoch of Reionization Window: Measurements of Foreground Isolation with PAPER. *ApJ*, 768:L36, May 2013.

[54] P. Procopio, R. B. Wayth, J. Line, C. M. Trott, H. T. Intema, D. A. Mitchell, B. Pindor, J. Riding, S. J. Tingay, M. E. Bell, J. R. Callingham, K. S. Dwarakanath, B.-Q. For, B. M. Gaensler, P. J. Hancock, L. Hindson, N. Hurley-Walker, M. Johnston-Hollitt, A. D. Kapińska, E. Lenc, B. McKinley, J. Morgan, A. Offringa, L. Staveley-Smith, C. Wu, and Q. Zheng. A High-Resolution Foreground Model for the MWA EoR1

Field: Model and Implications for EoR Power Spectrum Analysis. *PASA*, 34:e033, August 2017.

[55] G. Pupillo, G. Naldi, G. Bianchi, A. Mattana, J. Monari, F. Perini, M. Poloni, M. Schiaffino, P. Bolli, A. Lingua, I. Aicardi, H. Bendea, P. Maschio, M. Piras, G. Virone, F. Paonessa, Z. Farooqui, A. Tibaldi, G. Addamo, O. A. Peverini, R. Tascone, and S. J. Wijnholds. Medicina array demonstrator: calibration and radiation pattern characterization using a UAV-mounted radio-frequency source. *Experimental Astronomy*, 39:405–421, June 2015.

[56] A. C. S. Readhead, B. S. Mason, C. R. Contaldi, T. J. Pearson, J. R. Bond, S. T. Myers, S. Padin, J. L. Sievers, J. K. Cartwright, M. C. Shepherd, D. Pogosyan, S. Prunet, P. Altamirano, R. Bustos, L. Bronfman, S. Casassus, W. L. Holzapfel, J. May, U.-L. Pen, S. Torres, and P. S. Udomprasert. Extended Mosaic Observations with the Cosmic Background Imager. *ApJ*, 609:498–512, July 2004.

[57] M. Ryle and A. Hewish. The synthesis of large radio telescopes. *MNRAS*, 120:220, 1960.

[58] R. J. Sault, J. P. Hamaker, and J. D. Bregman. Understanding radio polarimetry. II. Instrumental calibration of an interferometer array. *A&AS*, 117:149–159, May 1996.

[59] T. W. Shimwell, C. Tasse, M. J. Hardcastle, A. P. Mechev, W. L. Williams, P. N. Best, H. J. A. Röttgering, J. R. Callingham, T. J. Dijkema, F. de Gasperin, D. N. Hoang, B. Hugo, M. Mirmont, J. B. R. Oonk, I. Prandoni, D. Rafferty, J. Sabater, O. Smirnov, R. J. van Weeren, G. J. White, M. Atemkeng, L. Bester, E. Bonnassieux, M. Brüggen, G. Brunetti, K. T. Chyży, R. Cochrane, J. E. Conway, J. H. Croston, A. Danezi, K. Duncan, M. Haverkorn, G. H. Heald, M. Iacobelli, H. T. Intema, N. Jackson, M. Jamrozy, M. J. Jarvis, R. Lakhoo, M. Mevius, G. K. Miley, L. Morabito, R. Morganti, D. Nisbet, E. Orrú, S. Perkins, R. F. Pizzo, C. Schrijvers, D. J. B. Smith, R. Vermeulen, M. W. Wise, L. Alegre, D. J. Bacon, I. M. van Bemmel, R. J. Beswick, A. Bonafede, A. Botteon, S. Bourke, M. Brienza, G. Calistro Rivera, R. Cassano, A. O. Clarke, C. J. Conselice, R. J. Dettmar, A. Drabent, C. Dumba, K. L. Emig, T. A. Enßlin, C. Ferrari, M. A. Garrett, R. T. Génova-Santos, A. Goyal, G. Gürkan, C. Hale, J. J. Harwood, V. Heesen, M. Hoeft, C. Horellou, C. Jackson, G. Kokotanekov, R. Kondapally, M. Kunert-Bajraszewska, V. Mahatma, E. K. Mahony, S. Mandal, J. P. McKean, A. Merloni, B. Mingo, A. Miskolczi, S. Mooney, B. Nikiel-Wroczyński, S. P. O'Sullivan, J. Quinn, W. Reich, C. Roskowiński, A. Rowlinson, F. Savini, A. Saxena, D. J. Schwarz, A. Shulevski, S. S. Sridhar, H. R. Stacey, S. Urquhart, M. H. D. van der Wiel, E. Varenius, B. Webster, and A. Wilber. The LOFAR Two-metre Sky Survey. II. First data release. *A&A*, 622:A1, February 2019.

[60] O. M. Smirnov. Revisiting the radio interferometer measurement equation. I. A full-sky Jones formalism. *A&A*, 527:A106, March 2011.

[61] O. M. Smirnov. Revisiting the radio interferometer measurement equation. II. Calibration and direction-dependent effects. *A&A*, 527:A107, March 2011.

[62] O. M. Smirnov. Revisiting the radio interferometer measurement equation. III. Addressing direction-dependent effects in 21 cm WSRT observations of 3C 147. *A&A*, 527:A108, March 2011.

[63] O. M. Smirnov and C. Tasse. Radio interferometric gain calibration as a complex optimization problem. *MNRAS*, 449:2668–2684, May 2015.

[64] M. Sokolowski, T. Colegate, A. T. Sutinjo, D. Ung, R. Wayth, N. Hurley-Walker, E. Lenc, B. Pindor, J. Morgan, D. L. Kaplan, M. E. Bell, J. R. Callingham, K. S. Dwarakanath, B.-Q. For, B. M. Gaensler, P. J. Hancock, L. Hindson, M. Johnston-Hollitt, A. D. Kapińska, B. McKinley, A. R. Offringa, P. Procopio, L. Staveley-Smith, C. Wu, and Q. Zheng. Calibration and Stokes Imaging with Full Embedded Element Primary Beam Model for the Murchison Widefield Array. *PASA*, 34:e062, November 2017.

[65] I. S. Sullivan, M. F. Morales, B. J. Hazelton, W. Arcus, D. Barnes, G. Bernardi, F. H. Briggs, J. D. Bowman, J. D. Bunton, R. J. Cappallo, B. E. Corey, A. Deshpande, L. deSouza, D. Emrich, B. M. Gaensler, R. Goeke, L. J. Greenhill, D. Herne, J. N. Hewitt, M. Johnston-Hollitt, D. L. Kaplan, J. C. Kasper, B. B. Kincaid, R. Koenig, E. Kratzenberg, C. J. Lonsdale, M. J. Lynch, S. R. McWhirter, D. A. Mitchell, E. Morgan, D. Oberoi, S. M. Ord, J. Pathikulangara, T. Prabu, R. A. Remillard, A. E. E. Rogers, A. Roshi, J. E. Salah, R. J. Sault, N. Udaya Shankar, K. S. Srivani, J. Stevens, R. Subrahmanyan, S. J. Tingay, R. B. Wayth, M. Waterson, R. L. Webster, A. R. Whitney, A. Williams, C. L. Williams, and J. S. B. Wyithe. Fast Holographic Deconvolution: A New Technique for Precision Radio Interferometry. *ApJ*, 759:17, November 2012.

[66] C. Tasse. Nonlinear Kalman filters for calibration in radio interferometry. *A&A*, 566:A127, June 2014.

[67] C. Tasse, S. van der Tol, J. van Zwieten, G. van Diepen, and S. Bhatnagar. Applying full polarization A-Projection to very wide field of view instruments: An imager for LOFAR. *A&A*, 553:A105, May 2013.

[68] A. Richard Thompson, James M. Moran, and Jr. Swenson, George W. *Interferometry and Synthesis in Radio Astronomy, 3rd Edition*. 2017.

[69] N. Thyagarajan, N. Udaya Shankar, R. Subrahmanyan, W. Arcus, G. Bernardi, J. D. Bowman, F. Briggs, J. D. Bunton, R. J. Cappallo, B. E. Corey, L. deSouza, D. Emrich, B. M. Gaensler, R. F. Goeke, L. J. Greenhill, B. J. Hazelton, D. Herne, J. N. Hewitt, M. Johnston-Hollitt, D. L. Kaplan, J. C. Kasper, B. B. Kincaid, R. Koenig, E. Kratzenberg, C. J. Lonsdale, M. J. Lynch, S. R. McWhirter, D. A. Mitchell, M. F. Morales, E. H. Morgan, D. Oberoi, S. M. Ord, J. Pathikulangara, R. A. Remillard, A. E. E. Rogers, D. Anish Roshi, J. E. Salah, R. J. Sault, K. S. Srivani, J. B. Stevens, P. Thiagaraj, S. J. Tingay, R. B. Wayth, M. Waterson, R. L. Webster, A. R. Whitney, A. J. Williams, C. L. Williams, and J. S. B. Wyithe. A Study of Fundamental Limitations to Statistical Detection of Redshifted H I from the Epoch of Reionization. *ApJ*, 776:6, October 2013.

[70] C. L. Van Eck, M. Haverkorn, M. I. R. Alves, R. Beck, P. Best, E. Carretti, K. T. Chyży, J. S. Farnes, K. Ferrière, M. J. Hardcastle, G. Heald, C. Horellou, M. Iacobelli, V. Jelić, D. D. Mulcahy, S. P. O'Sullivan, I. M. Polderman, W. Reich, C. J. Riseley, H. Röttgering, D. H. F. M. Schnitzeler, T. W. Shimwell, V. Vacca, J. Vink, and G. J. White. Polarized point sources in the LOFAR Two-meter Sky Survey: A preliminary catalog. *A&A*, 613:A58, June 2018.

[71] H. Vedantham, N. Udaya Shankar, and R. Subrahmanyan. Imaging the Epoch of Reionization: Limitations from Foreground Confusion and Imaging Algorithms. *ApJ*, 745:176, February 2012.

[72] M. White, J. E. Carlstrom, M. Dragovan, and W. L. Holzapfel. Interferometric Observation of Cosmic Microwave Background Anisotropies. *ApJ*, 514:12–24, March 1999.

[73] M. H. Wieringa. An investigation of the telescope based calibration methods 'redundancy' and 'self-cal'. *Experimental Astronomy*, 2:203–225, 1992.

[74] S. J. Wijnholds, T. L. Grobler, and O. M. Smirnov. Calibration artefacts in radio interferometry - II. Ghost patterns for irregular arrays. *MNRAS*, 457:2331–2354, April 2016.

[75] S. Yatawatta. Distributed radio interferometric calibration. *MNRAS*, 449:4506–4514, June 2015.

[76] S. Yatawatta, A. G. de Bruyn, M. A. Brentjens, P. Labropoulos, V. N. Pandey, S. Kazemi, S. Zaroubi, L. V. E. Koopmans, A. R. Offringa, V. Jelić, O. Martinez Rubi, V. Veligatla, S. J. Wijnholds, W. N. Brouw, G. Bernardi, B. Ciardi, S. Daiboo, G. Harker, G. Mellema, J. Schaye, R. Thomas, H. Vedantham, E. Chapman, F. B. Abdalla, A. Alexov, J. Anderson, I. M. Avruch, F. Batejat, M. E. Bell, M. R. Bell, M. Bentum, P. Best, A. Bonafede, J. Bregman, F. Breitling, R. H. van de Brink, J. W. Broderick, M. Brüggen, J. Conway, F. de Gasperin, E. de Geus, S. Duscha, H. Falcke, R. A. Fallows, C. Ferrari, W. Frieswijk, M. A. Garrett, J. M. Griessmeier, A. W. Gunst, T. E. Hassall, J. W. T. Hessels, M. Hoeft, M. Iacobelli, E. Juette, A. Karastergiou, V. I. Kondratiev, M. Kramer, M. Kuniyoshi, G. Kuper, J. van Leeuwen, P. Maat, G. Mann, J. P. McKean, M. Mevius, J. D. Mol, H. Munk, R. Nijboer, J. E. Noordam, M. J. Norden, E. Orru, H. Paas, M. Pandey-Pommier, R. Pizzo, A. G. Polatidis, W. Reich, H. J. A. Röttgering, J. Sluman, O. Smirnov, B. Stappers, M. Steinmetz, M. Tagger, Y. Tang, C. Tasse, S. ter Veen, R. Vermeulen, R. J. van Weeren, M. Wise, O. Wucknitz, and P. Zarka. Initial deep LOFAR observations of epoch of reionization windows. I. The north celestial pole. *A&A*, 550:A136, February 2013.

[77] H. Zheng, M. Tegmark, V. Buza, J. S. Dillon, H. Gharibyan, J. Hickish, E. Kunz, A. Liu, J. Losh, A. Lutomirski, S. Morrison, S. Narayanan, A. Perko, D. Rosner, N. Sanchez, K. Schutz, S. M. Tribiano, M. Valdez, H. Yang, K. Z. Adami, I. Zelko, K. Zheng, R. P. Armstrong, R. F. Bradley, M. R. Dexter, A. Ewall-Wice, A. Magro, M. Matejek, E. Morgan, A. R. Neben, Q. Pan, R. F. Penna, C. M. Peterson, M. Su, J. Villasenor, C. L. Williams, and Y. Zhu. MITEoR: a scalable interferometer for precision 21 cm cosmology. *MNRAS*, 445:1084–1103, December 2014.

[78] H. Zheng, M. Tegmark, J. S. Dillon, A. Liu, A. R. Neben, S. M. Tribiano, R. F. Bradley, V. Buza, A. Ewall-Wice, H. Gharibyan, J. Hickish, E. Kunz, J. Losh, A. Lutomirski, E. Morgan, S. Narayanan, A. Perko, D. Rosner, N. Sanchez, K. Schutz, M. Valdez, J. Villasenor, H. Yang, K. Zarb Adami, I. Zelko, and K. Zheng. Brute-force mapmaking with compact interferometers: a MITEoR northern sky map from 128 to 175 MHz. *MNRAS*, 465:2901–2915, March 2017.